


Research Paper

Therapeutic Fluorescent Hybrid Nanoparticles for Traceable Delivery of Glucocorticoids to Inflammatory Sites

Joanna Napp^{1,2}, M. Andrea Markus², Joachim G. Heck³, Christian Dullin^{1,2,4}, Wiebke Möbius⁵, Dimitris Gorpas⁶, Claus Feldmann³ and Frauke Alves^{1,2,7}

1. Institute of Diagnostic and Interventional Radiology, University Medicine Goettingen, Goettingen, Germany
2. Translational Molecular Imaging, Max-Planck Institute for Experimental Medicine, Goettingen, Germany
3. Institute of Inorganic Chemistry, Karlsruhe Institute of Technology, Karlsruhe, Germany
4. Italian Synchrotron "Elettra", Trieste, Italy
5. Department of Neurogenetics, Max-Planck Institute for Experimental Medicine, Goettingen, Germany
6. Institute of Biological and Medical Imaging, Helmholtz Zentrum Munich, Germany and Chair of Biological Imaging, Technical University of Munich, Germany
7. Clinic of Haematology and Medical Oncology, University Medicine Goettingen, Goettingen, Germany

 Corresponding authors: Prof. Frauke Alves (falves@gwdg.de), Translational Molecular Imaging, Max-Planck Institute for Experimental Medicine, Goettingen, Germany. Phone: 0049 (0) 551 3899 655; Fax: 0049 (0) 551 3899 644 & Dr. Joanna Napp, Ph.D. (jnowako1@gwdg.de; napp@em.mpg.de), Institute of Diagnostic and Interventional Radiology, University Medicine Goettingen, Goettingen, Germany. Phone: 0049 (0) 551 3899 272; Fax: 0049 (0) 551 3899 644

© Ivyspring International Publisher. This is an open access article distributed under the terms of the Creative Commons Attribution (CC BY-NC) license (<https://creativecommons.org/licenses/by-nc/4.0/>). See <http://ivyspring.com/terms> for full terms and conditions.

Received: 2018.07.05; Accepted: 2018.10.19; Published: 2018.12.07

Abstract

Treatment of inflammatory disorders with glucocorticoids (GCs) is often accompanied by severe adverse effects. Application of GCs via nanoparticles (NPs), especially those using simple formulations, could possibly improve their delivery to sites of inflammation and therefore their efficacy, minimising the required dose and thus reducing side effects. Here, we present the evaluation of NPs composed of GC betamethasone phosphate (BMP) and the fluorescent dye DY-647 (BMP-IOH-NPs) for improved treatment of inflammation with simultaneous *in vivo* monitoring of NP delivery.

Methods: BMP-IOH-NP uptake by MH-S macrophages was analysed by fluorescence and electron microscopy. Lipopolysaccharide (LPS)-stimulated cells were treated for 48 h with BMP-IOH-NPs (1×10^{-5} - 1×10^{-9} M), BMP or dexamethasone (Dexa). Drug efficacy was assessed by measurement of interleukin 6. Mice with Zymosan-A-induced paw inflammation were intraperitoneally treated with BMP-IOH-NPs (10 mg/kg) and mice with ovalbumin (OVA)-induced allergic airway inflammation (AAI) were treated intranasally with BMP-IOH-NPs, BMP or Dexa (each 2.5 mg/kg). Efficacy was assessed *in vivo* by paw volume measurements with μ CT and *ex vivo* by measurement of paw weight for Zymosan-A-treated mice, or in the AAI model by *in vivo* x-ray-based lung function assessment and by cell counts in the bronchoalveolar lavage (BAL) fluid and histology. Delivery of BMP-IOH-NPs to the lungs of AAI mice was monitored by *in vivo* optical imaging and by fluorescence microscopy.

Results: Uptake of BMP-IOH-NPs by MH-S cells was observed during the first 10 min of incubation, with the NP load increasing over time. The anti-inflammatory effect of BMP-IOH-NPs *in vitro* was dose dependent and higher than that of Dexa or free BMP, confirming efficient release of the drug. *In vivo*, Zymosan-A-induced paw inflammation was significantly reduced in mice treated with BMP-IOH-NPs. AAI mice that received BMP-IOH-NPs or Dexa but not BMP revealed significantly decreased eosinophil numbers in BALs and reduced immune cell infiltration in lungs. Correspondingly, lung function parameters, which were strongly affected in non-treated AAI mice, were unaffected in AAI mice treated with BMP-IOH-NPs and resembled those of healthy animals. Accumulation of BMP-IOH-NPs within the lungs of AAI mice was detectable by optical imaging for at least 4 h *in vivo*, where they were preferentially taken up by peribronchial and alveolar M2 macrophages.

Conclusion: Our results show that BMP-IOH-NPs can effectively be applied in therapy of inflammatory diseases with at least equal efficacy as the gold standard Dexa, while their delivery can be simultaneously tracked *in vivo* by fluorescence imaging. BMP-IOH-NPs thus have the potential to reach clinical applications.

Key words: hybrid nanoparticles, nanoparticle-based therapy, inflammatory disease, monitoring glucocorticoid delivery, *in vivo* imaging

Introduction

Inflammation is a primary defence mechanism against infection or injury, is required and beneficial, and is strictly coordinated by a wide range of mediators. If dysregulated, inflammation can turn into a chronic disease and can lead to tissue damage or even death. Inflammatory disorders such as autoimmune diseases, eczema, allergic asthma or food allergies are especially on the rise in the Western world [1]. One such inflammatory disorder, allergic asthma, is a chronic pulmonary disease characterised by a major influx of eosinophils into the lungs, degranulation of mast cells, an increased number of activated T-cells, mucus hypersecretion, airway obstruction and airway hyper-responsiveness. These events are orchestrated by a complex network of inflammatory mediators including chemokines, cytokines and growth factors [2].

Glucocorticoids (GCs) such as betamethasone or dexamethasone are routinely used as an effective anti-inflammatory therapy for chronic inflammatory diseases such as asthma because they are immunosuppressive and so inhibit many of the initial events in the inflammatory response. GCs modulate target gene expression by direct binding of the GC/GC receptor complex to GC-responsive elements in the promoter region of these genes or by interaction of this complex with other transcription factors. GCs thus inhibit recruitment of inflammatory cells by suppressing the production of chemotactic mediators and adhesion molecules, and/or they by suppressing inflammation by activating anti-inflammatory proteins [3–5]. Patients with acute severe asthma are usually treated systemically with GCs as first-line agent, whereas topical (i.e., inhaled) GCs are used for long-term management in patients with persistent asthma [6]. In particular, the long term use of systemic and/or high doses of GCs is associated with multiple severe adverse effects such as immunosuppression, hypertension, hyperglycemia, hydroelectrolytic disorders, adrenal insufficiency, weight gain, increased skin fragility, myopathy, osteoporosis, metabolic disturbances and mood changes [7].

Obviously, effective treatment of a disease depends on efficient and specific delivery of the therapeutic agent to the site of action. It has been previously shown that this can be improved by using nanocarriers such as nanoparticles (NPs), micelles or liposomes, which can, e.g., increase the solubility of otherwise insoluble drugs, enhance their bioavailability, extend circulation times, achieve accumulation at pathological sites or even allow drug delivery at controlled rates [8–10]. In recent years, this has led to the development of a number of NPs that have been successfully introduced into clinical routine. Among

them, nanoformulations with improved delivery of chemotherapeutics such as Doxil (PEGylated liposomal doxorubicin), Abraxane (nab-paclitaxel: *nanoparticle albumin-bound paclitaxel*) or the recently approved ONIVYDE (PEGylated liposomal irinotecan) [11,12] are significant drivers of the development of nanomedicine. NPs are also increasingly applied in connection with different diseases, e.g., in the treatment of fungal infections with AmBisome (liposomal Amphotericin B) [13] or as magnetic resonance imaging (MRI) contrast agents (iron-oxide NPs, such as Sienna+ or Ferumoxytol) [14]. Most of these substances are simple formulations based on clinically approved building blocks, which aim to improve the delivery, specificity and pharmacodynamics of already available therapeutics.

In this context, improved delivery of GCs to inflammatory sites in the lung using GC-containing nanoformulations could provide a rapid response, minimise the required dose by increasing the local drug concentration and decrease systemic side effects [15]. GC-based nanotherapeutics, in particular those based on liposomal formulations, have recently been explored for treatment of various inflammatory disorders such as arthritis [16] or multiple sclerosis [17] and have been shown to selectively target sites of inflammation as well as significantly improve treatment efficacy. Various attempts have been made to use NPs to improve GC transport to inflammation sites in asthmatic lungs [18,19], although none of these have reached the clinic yet.

NPs have the additional advantage that they may be combined into hybrid nanomaterials that fulfil several functions simultaneously. Such multi-modal or multi-functional NPs allow, e.g., for controlled drug release together with monitoring of treatment delivery. For this purpose, NPs can be loaded with multiple fluorescent dyes or used as MRI or CT contrast agents [14,20–22]. Recently, we have introduced inorganic-organic hybrid NPs (IOH-NPs) as a novel group of multifunctional NPs, which can easily incorporate versatile functions such as drug transport and delivery together with NP tracking using fluorescence imaging, MRI or photoacoustic imaging (PAI) [22–24]. Our previous *in vitro* findings that fluorescent IOH-NPs containing the GC betamethasone phosphate (BMP) are taken up by macrophages and efficiently reduce pro-inflammatory cytokine TNF α production in stimulated mouse macrophages made them attractive for *in vivo* applications [23]. We thus postulated that BMP-loaded IOH-NPs could act as immunosuppressive drugs for the treatment of inflammatory diseases, and we analysed them *in vivo* in a simple model of sterile paw inflammation and in a model of allergic airway

inflammation (AAI). Our results demonstrate that the efficacy of fluorescent BMP-IOH-NPs is significantly higher than that of soluble BMP and at least equal to that of the gold standard dexamethasone, while their delivery can be simultaneously tracked *in vivo* via fluorescence imaging. Interestingly, the NPs were specifically localized in alveolar and bronchial M2 macrophages, suggesting that these cells act as a reservoir from which the drugs are released into the surrounding tissue.

Methods

Preparation and characterisation of IOH-NPs

IOH-NPs are a saline composition with $[\text{ZrO}]^{2+}$ as an inorganic cation and one or more functional organic anions resulting in the general composition $[\text{ZrO}]^{2+}[\text{R}_{\text{function}}\text{OPO}_3]^{2-}$. The $[\text{ZrO}]^{2+}$ cation, which guarantees the insolubility of the IOH-NPs in water, is highly biocompatible and clinically approved [25,26]. The organic anion $[\text{R}_{\text{function}}\text{OPO}_3]^{2-}$ has certain functionalities such as fluorescence or pharmaceutical activity. BMP-IOH-NPs with the chemical composition $[\text{ZrO}]^{2+}[(\text{BMP})_{0.996}(\text{DUT})_{0.004}]^{2-}$ contain the anti-inflammatory agent betamethasone phosphate ($[\text{BMP}]^{2-}$) with an extraordinarily high loading of 81 wt% as well as a minor amount of the near-infrared-emitting dye-modified nucleoside triphosphate DY-647-dUTP ($[\text{DUT}]^{2-}$; λ_{Ex} 653 nm, λ_{Em} 672 nm). The IOH-NPs were prepared by admixing a solution of $\text{ZrOCl}_2 \cdot 8\text{H}_2\text{O}$ (5 mg, >99%, Sigma-Aldrich, Germany) in H_2O (2.5 mL) to a solution of sodium betamethasone 21-phosphate ($\text{Na}_2(\text{BMP})$, 50 mg, $\geq 97\%$, Sigma-Aldrich, Germany) in H_2O (50 mL) and the dye-modified nucleoside triphosphate DY-647-dUTP (1.2 mg in 100 μL of H_2O , Dyomics, Germany). IOH-NPs were then redispersed in dextran 40 (30 mM, pH = 7.4). The suspension contained 2.1 mg/mL $[\text{ZrO}]^{2+}[(\text{BMP})_{0.996}(\text{DUT})_{0.004}]^{2-}$ and 1.7 mg/mL BMP. At a pH of 6-8, $[\text{ZrO}]^{2+}[(\text{BMP})_{0.996}(\text{DUT})_{0.004}]^{2-}$ is highly insoluble in water. Thus, stirring of the NPs over 48 h at pH 7 (Hepes buffer) and 37 °C in the presence of acid phosphatase results in a BMP release of less than 5%. The synthesis, chemical composition, particle size, as well as the properties of the $[\text{ZrO}]^{2+}[(\text{BMP})_{0.996}(\text{DUT})_{0.004}]^{2-}$ IOH-NPs were described in detail before [23]. The presence of the fluorescent dye anion $[\text{DUT}]^{2-}$ in $[\text{ZrO}]^{2+}[(\text{BMP})_{0.996}(\text{DUT})_{0.004}]^{2-}$ was validated by fluorescence spectroscopy. For imaging of whole mouse cryosections, the fluorescent dye indocyanine green (ICG; λ_{Ex} 788 nm, λ_{Em} 813 nm) was used instead of DY-647 in order to meet the filter settings of the system.

Scanning electron microscopy (SEM) was carried out with a Zeiss Supra 40 VP (Zeiss, Germany)

equipped with a field emission gun (acceleration voltage 1 kV, working distance 3 mm). Samples were prepared by placing a droplet of diluted aqueous suspension of the sulfonate-based IOH-NPs on a silica wafer that was left to dry overnight.

Dynamic light scattering (DLS) was used to determine the hydrodynamic diameter of the BMP-IOH-NPs and their size distribution in suspension. Studies were conducted in polystyrene cuvettes using a Nanosizer ZS (Malvern Instruments, United Kingdom).

Zeta potential measurements were conducted using an automatic titrator MPT-2 attached to the Nanosizer ZS. For a typical measurement, 1 mL of a suspension containing 1 mg/mL of BMP-IOH-NPs was diluted with 9 mL of demineralized water. Titration was performed using 0.01 M and 0.1 M HCl as well as 0.01 M and 0.1 M NaOH.

Cells and cell culture

The immortalized and adherent mouse alveolar macrophage cell line MH-S (CRL-2019, ATCC) was cultivated at 37 °C in a humidified atmosphere of 5% CO_2 in complete RPMI medium supplemented with 10% fetal calf serum (FCS) and 0.05 mM 2-mercaptoethanol. To assess the anti-inflammatory potential of BMP-IOH-NPs *in vitro*, 2×10^5 MH-S cells were plated in 96-well plates in 200 μL medium per well and allowed to attach for 24 h. An inflammatory response was provoked with 200 ng/mL lipopolysaccharide (LPS, Sigma). Simultaneously, the cells were either treated with BMP-IOH-NPs or one of the control drugs dexamethasone (Dexa; Ratiopharm, Germany) or BMP (Sigma-Aldrich, Germany), each at concentrations of 1×10^9 to 1×10^5 M of active substance. After 48 h, the medium was collected and release of interleukin 6 (IL-6) into the culture medium was measured with the Mouse IL-6 ELISA Kit (Life Technologies, Germany), according to the manufacturer's protocol. The absorbance at 450 nm was measured with a Wallac 1420 Victor 2 Multilabel Counter (Perkin Elmer, Germany).

For toxicity analysis, MH-S cells were plated on 96-well plates (10,000 cells per well) and allowed to attach. On the following day, the medium was replaced with cell culture medium supplemented with increasing concentrations (1×10^9 to 1×10^5 M) of BMP-IOH-NPs, Dexa or BMP, or with corresponding volumes of PBS. Cell viability was measured after incubation for 2, 24, 48, and 72 h using a CellTiter 96 Aqueous One Solution Cell Proliferation Assay (Promega). The absorbance at 490 nm was measured using an Eon microplate spectrophotometer (BioTek).

For confocal fluorescence microscopy, MH-S cells were incubated for different times with 50

mg/mL of BMP-IOH-NPs, washed twice with phosphate buffered saline (PBS), and then fixed with 4% paraformaldehyde (PFA) for 10 min at room temperature (RT) before being counterstained and mounted with ProLong Gold Antifade Mountant with DAPI (Thermo Fisher Scientific, Germany). Fluorescence was visualized using a SP2 confocal microscope (Leica, Germany). 0.25 μm Z-stacks were acquired.

Electron microscopy

MH-S cells were incubated with 50 mg/mL of BMP-IOH-NPs for various incubation periods and fixed with 4% PFA/ 2.5% glutaraldehyde in 0.1 M PBS pH 7.3. The cells were then fixed in culture dishes with 1% OsO₄ (Science Services, Germany) in 0.1 M PBS and embedded in Epon (Serva, Germany) after dehydration with ethanol and en bloc staining with 1.5% uranyl acetate (Merck)/ 1.5% tungstophosphoric acid (Merck, Germany) in 70% ethanol. Ultrathin sections of cultured cells were cut parallel to the substrate using an UC7 Ultramicrotome (Leica, Germany) and stained with an aqueous solution of 4% uranyl acetate followed by lead citrate [27]. Sections were analysed with a LEO EM912 Omega (Zeiss, Germany) and digital micrographs were obtained with an on-axis 2048×2048 CCD camera (TRS).

Animals

Pathogen-free female immunocompetent BALB/c mice bred in-house and hairless SKH-1 mice (Charles River Laboratories Inc., Germany) were used for the Zymosan A-induced paw inflammation model and for AAI induction, respectively. Mice were housed in a controlled environment at a 12 h dark/light cycle and at 22 °C and were fed laboratory chow and tap water *ad libitum*. All animal experiments were performed in accordance with German animal ethics regulations and were approved by the local ethics office (Niedersächsisches Landesamt für Verbraucherschutz und Lebensmittelsicherheit, LAVES, ethics approval no. 33.14-42502-04-13/1185).

Induction of sterile paw inflammation and treatment schedule

To study the *in vivo* efficacy of the BMP-IOH-NPs, a sterile inflammation was induced at day 0 with a transcutaneous/intermuscular injection of Zymosan-A (Sigma; 500 μg in 50 μL PBS), an insoluble polysaccharide cell wall component of *Saccharomyces cerevisiae*, into the left hind paw of BALB/c mice [28]. The contralateral control paw was injected with 50 μL of PBS. Two hours later, mice were intraperitoneally (i.p.) injected either with BMP-IOH-NPs (10 mg/kg body weight (BW); n=7) or with the corresponding volume of 0.9% NaCl (n=6) and the treatment was repeated on days 1, 2 and 3. Animals

were sacrificed on day 4 by isoflurane overdose and cervical dislocation, and hind paws were isolated at a defined position and weighed.

In vivo micro computed tomography (μCT)

To quantify the paw volumes, *in vivo* μCT was performed on day 0 before the start of the treatment as well as at the end of the study on day 4. Scans were carried out under gas anaesthesia (~2% isoflurane in 2 L/min O₂/air mix 50%/50%), with a low-dose *in vivo* μCT (Quantum FX, Perkin Elmer) using the following parameters: 70 kVp, 200 μA and a field of view (FOV) of 40×40 mm. 3D image visualization and volumetric analyses were performed using the 3D analysis software Scry v6.0 (Kuchel & Sautter). For volume calculation, paws were virtually isolated from the centre point between the distal end of the tibia and the junction between tibia and fibula and the total volume was calculated using a simple threshold-based method to separate the surrounding air from the tissue.

Induction of AAI and treatment schedule

On days 0 and 14, mice were immunized by i.p. injection with 50 μg of ovalbumin (OVA, Hyglos, Germany) and 0.5% aluminium hydroxide gel adjuvant (Invivogen, Germany) in a volume of 0.2 mL of PBS, as well as intranasally (i.n.) with 50 μg of OVA in 25 μL of PBS. On days 28 and 29, mice were challenged i.n. with 250 μg of OVA in 25 μL of PBS to induce an acute reaction. For control mice, OVA was replaced with PBS in the immunisation steps on days 0 and 14.

Mice were treated i.n. with BMP-IOH-NPs, BMP or Dexa, each at 2.4 mg of active substance per kg BW. The substances were diluted in 0.9% NaCl and 1.43 $\mu\text{L/g}$ BW was applied. Control animals received corresponding volumes of 0.9% NaCl. Treatment was given on days 28 and 29, each 30 min before the challenge, as well as on day 30. The ICG-containing BMP-IOH-NPs (2.4 mg BMP/kg BW) as well as the free DY-647 dye (13.97 $\mu\text{g/kg}$ BW; corresponds to the amount of dye in BMP-IOH-NPs) were applied using the same schedule. All i.n. applications were performed under short 2% isoflurane, 2 L/min O₂ anaesthesia. Mice were sacrificed on day 31 by isoflurane overdose and cervical dislocation and the lungs were either cannulated and lavaged or were directly explanted, filled with 600 μL of Tissue-Tek OCT compound (Sakura Finetek, The Netherlands), and frozen in liquid nitrogen.

In vivo fluorescence reflectance imaging

BMP-IOH-NPs fluorescence was measured with the Optix MX2 system (ART, Canada) using an excitation laser diode of 635 nm in combination with a

670 nm band-pass emission filter with 40 nm bandwidth. Scans of the lung area were performed with a 1.0 mm raster, a photon collection time (integration time) of 1 s per scan point, and varying laser power. During *in vivo* scans, mice were anaesthetized by inhalation with 2% isoflurane in 2 L/min O₂ for 15-30 min per scan. Pre-treatment scans were acquired to assess autofluorescence of the animals. Optix 2.02.01 and OptiView 2.01.00 software (ART) were used to acquire and analyse the data, respectively. Fluorescence intensity data were displayed in arbitrary units (normalized counts; NC), where the measured fluorescence intensities (counts) were normalized for varying laser power and integration times, allowing for comparison of measurements with different settings. Fluorescence lifetime was assessed as previously described [29].

In vivo assessment of lung function

Low-dose x-ray-based *in vivo* lung function measurement (XLF) was performed as previously described by Dullin et al. [30]. Briefly, mice were anaesthetised with isoflurane and the anaesthesia was adjusted to keep the breathing rate to approximately 1.4 s per breathing cycle. Cinematic x-ray images (1024 images) were acquired continuously with a rate of 30 images per second with a QuantumFX μ CT (Perkin Elmer) using the following parameters: FOV 20×20 mm², x-ray tube voltage 90 kVp and tube current 40 μ A, resulting in an entrance dose of about 6 mGy. Data was analysed using the software XLF [30]. The dynamic parameter $t_{in}[\%]$ represents the relative inhalation time, meaning the ratio of inhalation time to total length of a breathing event.

For diaphragm motion analysis, the average and the standard deviation (SD) of the changes in brightness for each pixel over time was calculated from the acquired x-ray movies using FIJI (National Institutes of Health, Bethesda, USA) [31]. Thereby, moving areas at the interface of dark and bright regions between the lungs and soft tissues beneath the lung, which we defined as the diaphragm, show very high SDs compared to static areas [32]. The average height of the area with high SD was measured at six independent positions (three per side) and was used as a parameter representing the average diaphragm movement (S_{dia}).

Bronchoalveolar lavage (BAL)

The trachea of the sacrificed mice was exposed and cannulated. BALs were performed by washing the airways gently three times with 500 μ L of 2% FCS/PBS each. Volumes were pooled and washed once with the same buffer. Recovered cells were counted and approximately 3×10⁴ cells were used for

cytospins utilising a Shandon Cytospin 4 (Thermo Fisher Scientific, Germany), and then stained with Giemsa (Sigma-Aldrich) for differential cell counting. Approximately 400-500 cells were counted and classified as macrophages, eosinophils, neutrophils or lymphocytes based on staining colour and characteristic morphology.

Histology, immunofluorescence staining and fluorescence microscopy

For histology, paws were fixed with 4% formalin in PBS (pH 7.4) overnight, washed with water and incubated with 10% EDTA, 3.3% Tris (pH 7.3) at 4 °C for 4-12 weeks. The EDTA/Tris solution was exchanged every few days and the progress of decalcification was assessed with a cannula. Decalcified paws were washed several times with PBS, dehydrated, washed, paraffin embedded, sectioned and stained with hematoxylin-eosin (H&E).

Cytospins from BALs were fixed with 1:1 acetone/methanol solution and stained with Giemsa or immunostained. Frozen lung sections of 5 μ m were fixed with acetone and stained with H&E in order to evaluate the degree of lung-infiltration with mononuclear cells, or pre-treated with 0.3 M glycine before using avidin-biotin block and Seablock (Thermos Scientific) for immunohistochemistry. For the detection of macrophages, cytospins and lung cryosections were stained with rat anti-mouse CD68 antibody (clone FA-11, Abcam, 1:300), followed by incubation with biotinylated goat anti-rat antibody (BioLegend, 1:200) and streptavidin-Alexa Fluor 488 (Life Technologies, 1:400). CD11c cell expression was assessed on lung sections with Alexa Fluor 488-conjugated anti-mouse CD11c (clone N418, BioLegend, 1:200) and MHCII expression was evaluated with Alexa Fluor 488-conjugated rat anti-mouse MHCII antibody (clone M5/114.15.2, Biolegend, 1:200). ECF-L was stained with a polyclonal goat anti-mouse ECF-L antibody (R&D, 1:150), followed by donkey anti-goat Alexa Fluor 488 secondary antibody (Abcam, 1:400). Eosinophils were identified by staining with rat anti-mouse Siglec-F antibody (clone e50-2440; BD Pharmingen), followed by goat-anti-rat biotin, and detection with avidin Alexa Fluor 488 (Molecular Probes). Hamster anti-mouse podoplanin (Santa Cruz Biotechnology, 1:200), followed by goat anti-hamster Alexa Fluor 488 secondary antibody (Life Technologies, 1:400) and rabbit anti-mouse prosurfactant Protein C (proSP-C) antibody (Millipore, 1:2000), followed by goat anti-rabbit Alexa Fluor 488 (Life Technologies, 1:400) were used to detect pulmonary alveolar type I (AT1) and type II (AT2) cells, respectively. All sections were co-stained with DAPI (4 μ g/mL) for visualization of nuclei and mounted

with Aqua-Poly/Mount (Polysciences).

Images were acquired with a confocal SP-2 microscope (Leica) and processed with FIJI [31].

Imaging of whole mouse cryosections

One AAI mouse treated with ICG-loaded BMP-IOH-NPs was sacrificed and tracheotomised. The lung was filled with a mixture of Tissue-Tek and black ink (8% w/w) and the entire mouse was embedded in a mixture of Tissue-Tek and black ink (8% w/w) and frozen. Whole-body cryosectioning in transversal planes was performed using a Leica CM 3500 cryostat at 20 μm steps. A custom-made imaging system was utilized to image the remaining block of the specimen after every section. Three reflectance images were acquired at 630/60 nm (red channel), 535/38 nm (green channel), and 460/50 nm (blue channel) for colour imaging as well as one fluorescence image at 810/90 nm (ET810/90, Chroma Technology) to capture the main part of the emission spectrum of the fluorophore. Additional fluorescence images were acquired at 790/10 nm, 810/10 nm, 830/20 nm, and 860/10 nm (Chroma Technology). These data were employed to segment the ICG emission from tissue autofluorescence and food fluorescence by applying phasor analysis [33,34]. The filters were placed in a custom-made motorized filter-wheel in the lens-camera path. A halogen light source (KL2500, Schott) coupled to fibre bundles and a motorized filter-wheel (FW102C, Thorlabs) illuminated the specimen. Reflectance images were enabled by white-light illumination (i.e., no light source filtering), whereas the fluorescence was excited by a fibre-coupled near-infrared (NIR 750 nm, 300 mW) continuous-wave diode laser (BWF2-750-0, B&W Tek). A Leica Z16 Apo Macroscope projected the image onto the sensor of an iXon electron-multiplying CCD camera (EMCCD, DV8201-BV, Andor Technology). The FOV was adjusted to cover the full-body cutting plane. Cutting and image-acquisition was automated. The sectioning and imaging system control and triggering software was developed with LabView (National Instruments) [35]. Data analysis was implemented in MATLAB (Mathworks).

Statistical analysis

Statistical analysis was performed with PAST [36]. Significant differences of the mean values between two groups were analysed by Student's *t*-test, with a p-value of 0.1 as the margin for statistical significance. All diagrams show mean values \pm SEM.

Results

In vitro characterisation of BMP-IOH-NPs

The BMP-IOH-NPs applied here have the

composition $[\text{ZrO}]^{2+}[(\text{BMP})_{0.996}(\text{DUT})_{0.004}]^{2-}$ and contain the anti-inflammatory agent betamethasone phosphate ($[\text{BMP}]^{2-}$) as well as the near-infrared-emitting dye-modified nucleoside triphosphate DY-647-dUTP ($[\text{DUT}]^{4-}$) (Figure 1A, left). The presence of the fluorescent dye anion $[\text{DUT}]^{2-}$ was confirmed by fluorescence spectroscopy (data not shown). Specific advantages of the BMP-IOH-NPs include a straightforward aqueous synthesis, simple composition and an unprecedentedly high drug load of 81 wt% BMP. In the presence of phosphatases, BMP is slowly released from the IOH-NPs via metabolic activity within 1-3 days. Electron microscopy revealed that the BMP-IOH-NPs exhibit a mean particle diameter of 31 ± 10 nm (Figure 1A, middle). In water, nanoparticles generally show larger hydrodynamic radii due to a rigid layer of adsorbed solvent molecules. Based on its high polarity and extensive hydrogen bonding networks, this rigid solvent layer is largely expanded in water resulting in hydrodynamic diameters of 40-60 nm (Figure 1A, middle). Aqueous suspensions exhibit a high colloidal stability, which can be ascribed to a negative surface charge as indicated by a zeta potential of -40 mV at pH 6 to 8 (Figure 1A, right). For a detailed characterization of $[\text{ZrO}]^{2+}[(\text{BMP})_{0.996}(\text{DUT})_{0.004}]^{2-}$ IOH-NPs, refer to our previously published data [23].

To investigate the cellular uptake of BMP-IOH-NPs, we incubated mouse alveolar MH-S macrophages with the NPs for different periods (10 min to 24 h) and analysed the cells with confocal fluorescence and electron microscopy. As shown in Figure 1B, NP-derived fluorescence was detectable in the cells as early as 10 min after incubation and increased over time, resulting in a high cell load after 24 h and thus demonstrating that BMP-IOH-NPs are effective vehicles for glucocorticoid delivery into the cells. This was confirmed by electron microscopy, which clearly showed that NPs are internalised within the first 10 min and are localised in large vesicles within the cells (Figure 1C).

To assess the efficacy of BMP-IOH-NPs *in vitro*, MH-S macrophages were stimulated with the endotoxin lipopolysaccharide (LPS) and treated for 48 h with BMP-IOH-NPs or with the reference soluble drugs, BMP and Dexa. The inflammatory response of the cells was assessed by quantifying IL-6 cytokine release into the cell culture medium. As shown in Figure 1D, all drugs effectively reduced IL-6 release in a concentration-dependent manner. The anti-inflammatory response of BMP-IOH-NPs was even stronger than that of the reference drugs, especially at lower concentrations (1×10^{-7} and 1×10^{-8} M). This confirmed that BMP-IOH-NPs are not only effectively internalised by the cells but evidently also

released their BMP drug load. This is in agreement with our previously published data [23], where we have shown that $[ZrO]^{2+}[(BMP)_{0.996}(DUT)_{0.004}]^{2-}$

resulted *in vitro* in a dose-dependent reduction of pro-inflammatory cytokine TNF α secretion from LPS-stimulated MH-S macrophages.

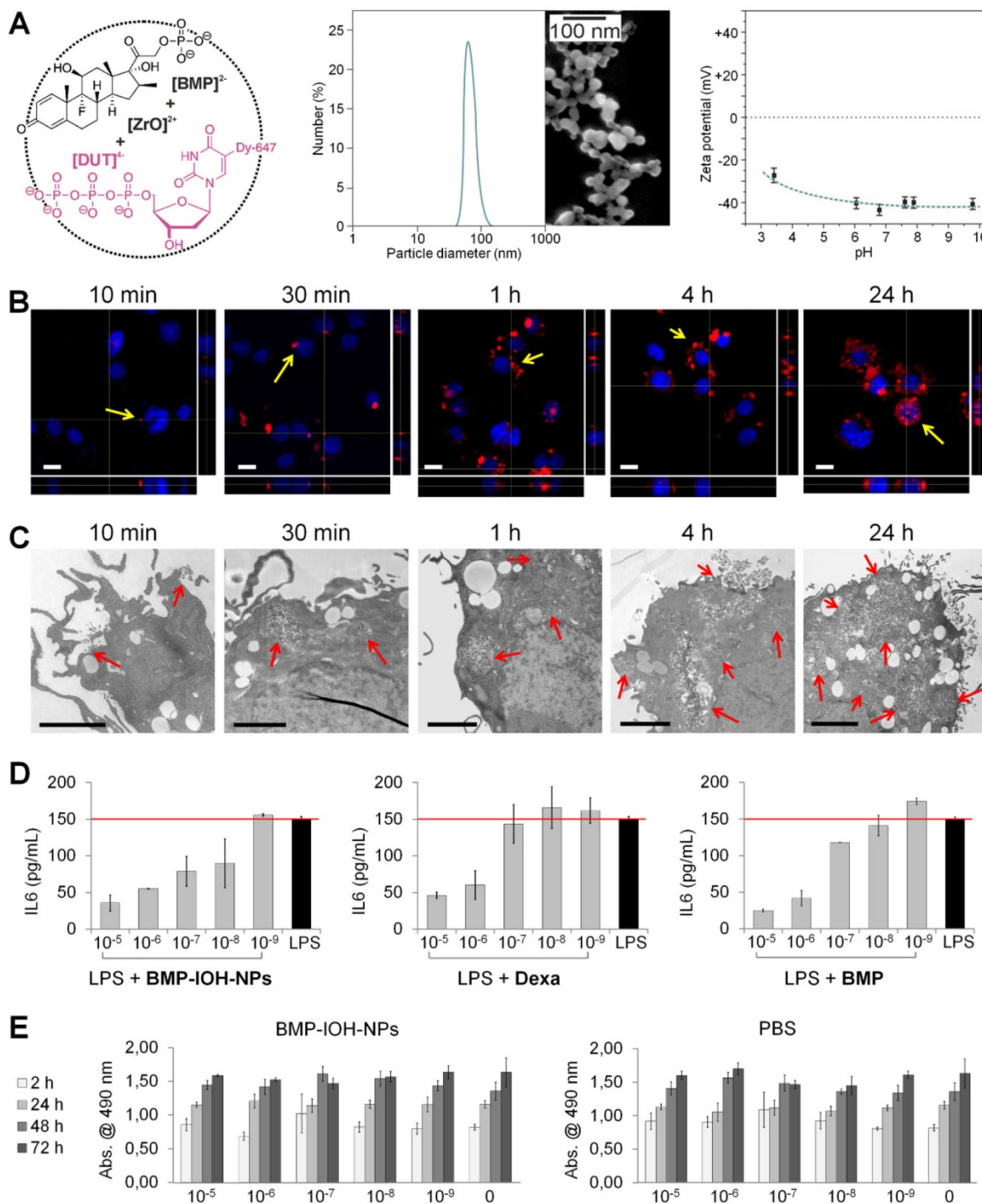


Figure 1. In vitro characterisation of BMP-IOH-NPs. (A) Features of BMP-IOH-NPs. Left: scheme illustrating the chemical composition $[ZrO]^{2+}[(BMP)_{0.996}(DUT)_{0.004}]^{2-}$ and aqueous synthesis; middle: electron microscopy image illustrating a particle size of 31 ± 10 nm; right: zeta potential in mV and its dependence on pH. (B-C) *In vitro* uptake of BMP-IOH-NPs by mouse alveolar MH-S macrophages analysed at different times of incubation by (B) confocal fluorescence microscopy with orthogonal projections (red: BMP-IOH-NPs, blue: nucleic stain (DAPI); scale bar 20 μ m) and by (C) electron microscopy (scale bar 2 μ m). Internalisation is detectable as early as 10 min of incubation and the NP load increased continuously over 24 h (arrows). (D) Efficacy of the BMP-IOH-NP in comparison to the control drugs BMP or Dexa (each 1×10^{-5} – 1×10^{-9} M of the active substance) on LPS-stimulated MH-S cells assessed by measurement of IL-6 level in the cell supernatant after 48 h of treatment. The anti-inflammatory effect of BMP-IOH-NPs on MH-S cells was dose dependent and comparable to that of Dexa and BMP, confirming efficient release of the drug from the NPs. Red lines show the mean IL-6 level in the non-treated LPS-stimulated cells. (E) Metabolic activity of MH-S murine macrophages after cultivation for 2, 24, 48, and 72 h with BMP-IOH-NPs or with corresponding volumes of PBS. Measurements were performed in triplicates; error bars correspond to standard deviation.

Despite substantial internalization and strong anti-inflammatory activity, BMP-IOH-NPs had no effects on the viability and/or metabolic activity of MH-S cells, as assessed by cell proliferation assays (**Figure 1E**). Cells treated for up to 72 h with increasing amounts of BMP-IOH-NPs showed the same behaviour as untreated cells or cells treated with corresponding amounts of PBS. Similarly, both Dexamethasone and BMP had no negative effects on the viability of MH-S cells (data not shown).

BMP-IOH-NPs effectively reduce sterile paw inflammation

To study the anti-inflammatory efficacy of BMP-IOH-NPs *in vivo*, we first applied them in a sterile model of paw inflammation, which allows the simple

assessment of the anti-inflammatory potential of novel drugs. The sterile inflammation was induced by a single transcutaneous/intramuscular Zymosan A injection into the left paws of BALB/c mice, which led to the development of paw oedema, whereas contralateral paws injected with the same volume of PBS did not show any swelling of the tissue (**Figure 2A-B**). Starting at 2 h post Zymosan A injection, mice were treated intraperitoneally (i.p.) daily for 4 days with BMP-IOH-NPs (10 mg/kg BW of active substance), whereas controls received corresponding volumes of 0.9% NaCl. Mice treated with BMP-IOH-NPs showed no obvious toxic effects, no weight loss and an overall good condition (data not shown).

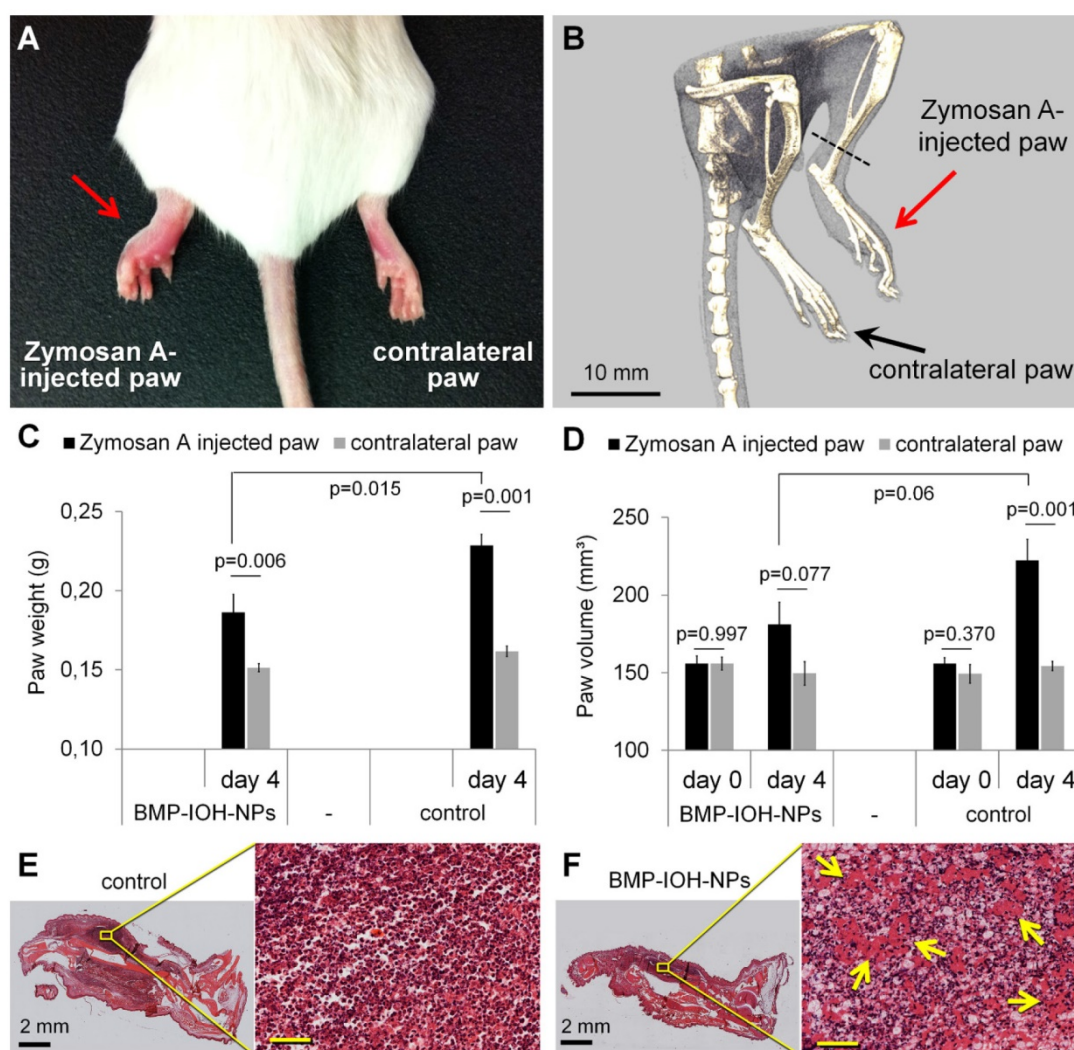


Figure 2. Evaluation of the *in vivo* anti-inflammatory effect of BMP-IOH-NPs in a sterile model of paw inflammation. (A) Macroscopic appearance and **(B)** representative μ CT-scan of a non-treated control mouse showing the development of oedema in the Zymosan A-injected but not in the contralateral PBS-injected paw. **(C)** The paw weights determined at the end of the experiment (day 4) showed significantly lower ($p=0.015$) development of Zymosan A-induced paw oedema in BMP-IOH-NPs-treated mice ($n=7$) than in the control group ($n=6$). **(D)** Paw volumes of the same mice measured *in vivo* by μ CT before treatment (day 0) and at the end of the experiment (day 4) confirmed the significant reduction on paw swelling in the BMP-IOH-NPs-treated mice in comparison to the controls ($p=0.06$). Contralateral PBS-injected paws all had comparable values of weights/volumes and did not show any swelling. Data are presented as mean values; error bars represent SEM. * corresponds to $p<0.1$ analysed by Student's *t*-test (PAST). **(E-F)** Representative H&E-stained sections of Zymosan A-injected paws from mice treated with **(E)** 0.9% NaCl (controls) and **(F)** BMP-IOH-NPs. Reduction of immune cells infiltration and the presence of exudate in the intercellular spaces in response to BMP-IOH-NPs treatment are shown in higher magnification and are labelled with arrows. Scale bars in the insets of **(E-F)**: 100 μ m.

As shown in **Figure 2C-D**, the oedema development in Zymosan A-injected paws was clearly reduced by BMP-IOH-NPs. At the time of dissection, the paws had significantly lower weights (**Figure 2C**) than those from control mice (0.186 ± 0.011 g vs. 0.228 ± 0.007 g; $p=0.015$). In accordance, mice treated with BMP-IOH-NPs also showed clearly reduced volumes due to a lesser extent of paw swelling (from 155.9 ± 5 mm³ at day 0 to 181.1 ± 14.2 mm³ at day 4) in comparison to the control group (from 155.9 ± 3.8 mm³ at day 0 to 222.4 ± 13.6 mm³), although the difference was not statistically significant ($p=0.06$; **Figure 2D**). The contralateral PBS-injected paws did not develop any oedema and were not affected by the treatment with BMP-IOH-NPs or 0.9% NaCl and at the time of the dissection showed almost identical weights (0.151 ± 0.002 g vs. 0.162 ± 0.003 g) and volumes (149.5 ± 7.5 mm³ vs. 154.3 ± 3.0 mm³).

Histological analyses showed a dense infiltration of mononuclear cells and severe inflammation of soft tissue in the Zymosan A-injected paws of control 0.9% NaCl-treated mice (**Figure 2E**). In comparison, the cell mass detected at sites of inflammation of the treated group was significantly reduced in density and exudate was present in the intercellular spaces, suggesting a reduction of the inflammatory process in response to BMP-IOH-NPs (**Figure 2F**).

Effects of BMP-IOH-NPs treatment on the inflammatory response of the lung

We then went on to test the treatment efficacy of BMP-IOH-NPs in a mouse model of allergic airway inflammation (AAI) using hairless immunocompetent SK-H mice, which facilitate the assessment of the potential of these NPs for *in vivo* tracking by fluorescence imaging.

In a series of four independent experiments, AAI was induced by using a conventional OVA protocol (**Figure 3A**) [37]. Mice were treated intranasally (i.n.) with either BMP-IOH-NPs or with the reference drugs Dexamethasone or BMP, each at a concentration of 2.4 mg of active substance per kg BW. Control groups of healthy and AAI mice were treated i.n. with the same volume of PBS. The distribution of BMP-IOH-NPs in the AAI lungs was monitored by *in vivo* epi-fluorescence imaging 1 h and 4 h after treatment as well as at the end of the experiment, 24 h after the last NP application. Here too, the overall condition of the treated animals was good, with no weight loss during the experiment (data not shown).

Before application to the animals, we measured the average fluorescence lifetime of the BMP-IOH-NPs *in vitro* to be ~ 1.7 ns (**Figure 3B**). *In vivo* accumulation of the BMP-IOH-NPs in the lung was clearly visible as early as 1 h after instillation and was

still detectable at 4 h but was usually strongly decreased at 24 h (**Figure 3C**). Additionally, accumulation of BMP-IOH-NPs was frequently detected in the area of the pharynx/trachea (**Figure 3C**) at early time points after injection (1-4 h; **Figure 3C**) and most probably resulted from some entrapment of NPs in the mucus during i.n. instillation. Interestingly, at 1 h post NP instillation, along with the NP-derived fluorescence detectable in the lung, a slight homogenous increase in background fluorescence was measured throughout the entire scanned area. This background signal had a probe-specific lifetime ($\sim 1.6 - 1.7$ ns) and was no longer observed in scans performed 4 h post instillation. At this time point, the BMP-IOH-NP-specific lifetime was only detectable over the lung area (**Figure 3C**). As fluorescence lifetime is independent of dye/particle concentration, we believe that a small part of BMP-IOH-NPs or decomposed NPs/fluorescent dye passively or actively reached circulation. This would result not only in a slight increase in the whole-body fluorescence intensity, but also in a probe-specific lifetime, as measured over the entire scanned area 1 h after NP application. 4 h and 24 h after NP application, the BMP-IOH-NP-derived lifetime was only detectable over the areas with a high fluorescence intensity, e.g., the lung, suggesting that at later time points no or negligible NPs/dye was present in the circulation (**Figure 3C**).

In all AAI mice, we observed a significant increase in the total number of cells recovered by BAL when compared to control mice that received 0.9% NaCl ($6.33 \pm 0.89 \times 10^5$ vs. $2.53 \pm 0.41 \times 10^5$; **Figure 4A, left**). Treatment of AAI mice with BMP-IOH-NPs significantly ($p=0.03$) reduced the total cell number in the lavages to $4.09 \pm 0.52 \times 10^5$. As expected, a similar cell count was found in AAI mice treated with the control drug Dexamethasone, ($4.40 \pm 0.84 \times 10^5$), although the difference was not statistically significant when compared to untreated AAI mice ($p=0.13$). Interestingly, treatment of AAI mice with soluble BMP did not affect the total cell count in the lavage ($6.12 \pm 1.0 \times 10^5$; $p=0.87$). The effects of the different treatments were even more prominent for the eosinophil counts in the lung lavage (**Figure 4A, middle**). While BALs from healthy controls contained a negligible amount of eosinophils (87 ± 87), induction of AAI with OVA resulted, as expected, in a significant increase in the total eosinophil numbers ($2.65 \pm 0.86 \times 10^5$; $p=0.00012$). While AAI mice treated with BMP-IOH-NPs and with Dexamethasone had significantly fewer eosinophils in their BALs than mice from the untreated AAI group ($0.77 \pm 0.29 \times 10^5$; $p=0.005$ and $0.41 \pm 0.16 \times 10^5$; $p=0.004$, respectively), the soluble BMP had almost no effect on the AAI-induced

eosinophilia, which remained at an average of $2.44 \pm 0.74 \times 10^5$ eosinophils ($p=0.84$). The total number of macrophages (Figure 4A, right) in the BAL of AAI mice ($3.17 \pm 0.28 \times 10^5$) was slightly higher than that in the healthy control mice ($2.49 \pm 0.41 \times 10^5$) and was not significantly affected by any treatment, with $3.03 \pm 0.31 \times 10^5$, $3.47 \pm 0.48 \times 10^5$ and $3.23 \pm 0.25 \times 10^5$ in the BMP-IOH-NPs-, Dexa- and BMP-treated mice, respectively. While macrophages accounted for $98\% \pm 0.3\%$ of total BAL cells in the healthy control mice,

they accounted for $56\% \pm 2.5\%$ of total cells in the AAI mice.

The different treatment effects were confirmed by histology of lung slices (Figure 4B), which showed strong infiltration of the lungs of AAI mice with immune cells, which was not detectable in healthy controls. This infiltration was strongly reduced in mice treated with both BMP-IOH-NPs and Dexa but was still present in mice who received soluble BMP.

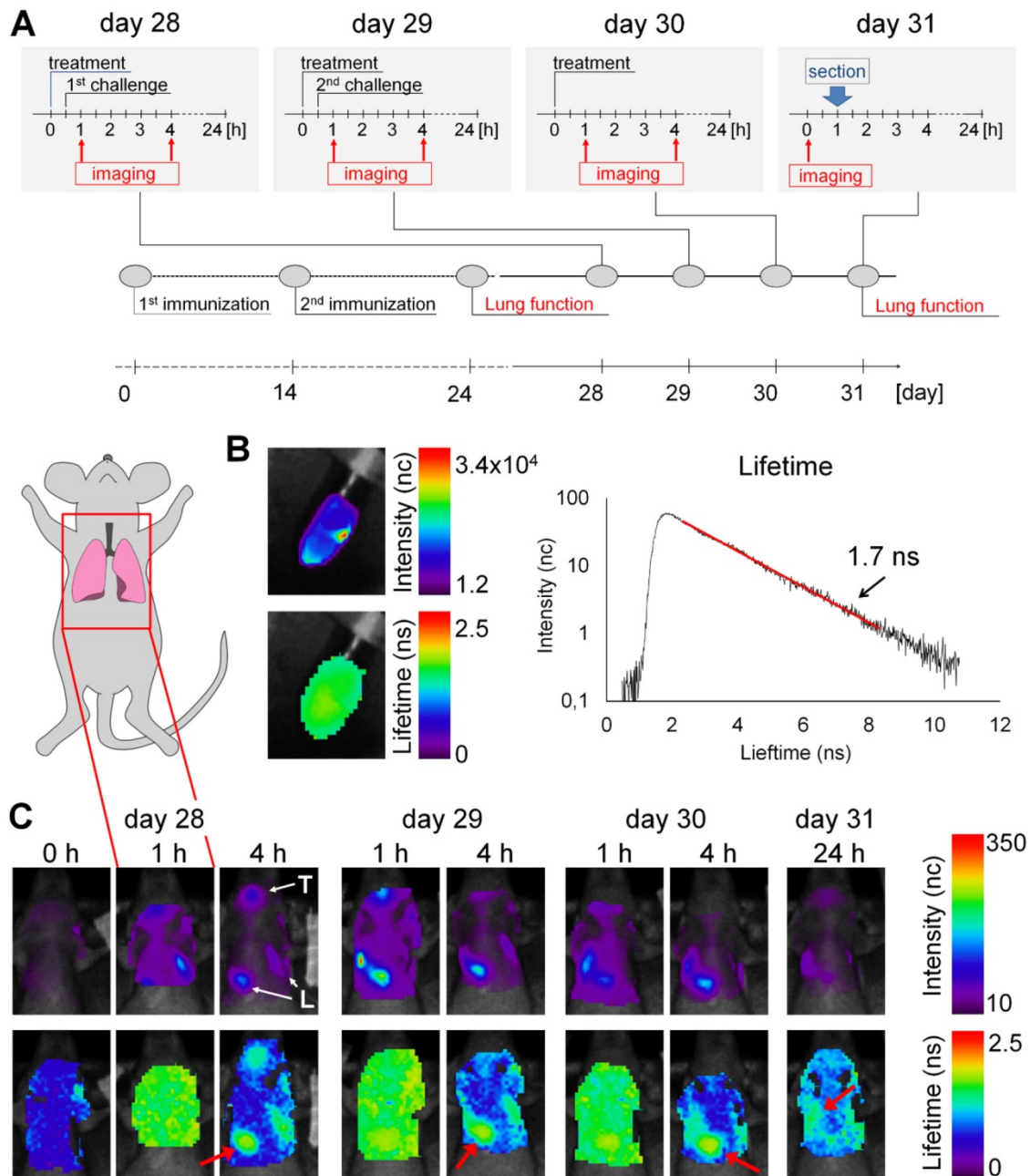


Figure 3. Accumulation of BMP-IOH-NPs in the lungs of AAI mice monitored by epi-fluorescence imaging *in vivo*. (A) Immunization and challenge scheme for the AAI model and experimental setup for treatment and imaging. (B) *In vitro* scan of BMP-IOH-NPs stock solution showing fluorescence intensity (upper panel) and lifetime (lower panel), as well as a representative photon time of flight histogram (right) used for the automatic calculation of the fluorescence lifetime (1.7 ns). (C) *In vivo* scans of the lung area (indicated with the inset on the mouse cartoon) before (0 h), 1 h and 4 h (days 28–30) as well as 24 h (day 31) after i.n. instillation of BMP-IOH-NPs. Upper panel: fluorescence intensity in normalised counts (nc); lower panel: lifetime in nanoseconds (ns). High fluorescence intensity was observed in the area of the pharynx/trachea (T) and lung (L). A homogeneous distribution of the probe-derived lifetime of ~1.6–1.7 ns was found throughout the scanned area at 1 h post instillation. At later time points the specific lifetime was only detectable over the lung area (red arrow).

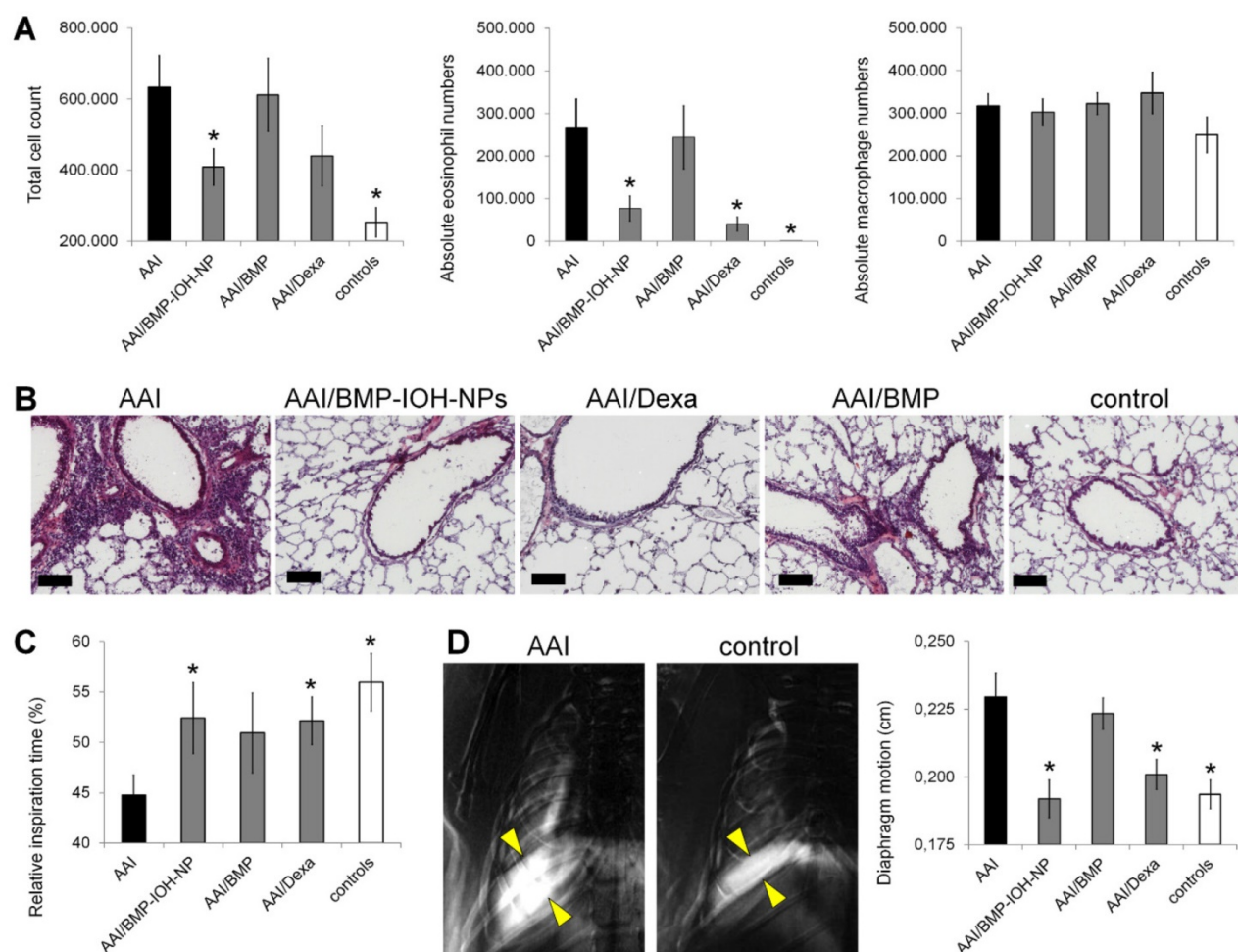


Figure 4. *In vivo* assessment of the efficacy of BMP-IOH-NPs in the AAI mouse model. **(A)** Total cell counts (left), eosinophils (middle) and macrophages (right) recovered by BAL from AAI SKH-1 mice treated with PBS (AAI), BMP-IOH-NPs (AAI/BMP-IOH-NPs), soluble BMP (AAI/BMP) or Dexamethasone (AAI/Dexa) as well as from healthy controls. **(B)** Corresponding H&E staining showing that BMP-IOH-NPs and Dexa, but not BMP, strongly reduced the degree of cell infiltration around blood vessels and bronchi in AAI mice to levels comparable to those of controls. Scale bars: 100 μ m. **(C)** XLF-based *in vivo* analysis of the relative inspiration time upon different treatments. **(D)** Diaphragm motion analysis. Left: representative images showing the SD of x-ray attenuation over time during breathing in a AAI and a control mouse. The white colour corresponds to a high SD, representing moving areas over time. Yellow arrows mark the motion amplitude of the lung-diaphragm interface. Right: analysis of the diaphragm motion upon different treatments. (A, C-D) Data are presented as mean values; error bars represent SEM. Significance was analysed in comparison to AAI mice. * corresponds to $p < 0.1$.

Alterations in lung function were assessed *in vivo* by x-ray-based lung function (XLF) analysis [30,32], a method based on parameterization of the average x-ray transmission in the chest region using low-dose planar cinematic radiography. We investigated two selected XLF parameters: the relative inspiration time, and the movement of the diaphragm. As shown in **Figure 4C**, the relative inspiration time, which depicts the ratio of inspiration time to average length of the breathing cycle ($t_{in}[\%]$), was strongly and significantly reduced in AAI mice when compared to healthy controls. This reduction was not obtained in AAI mice treated with any of the three treatments, although for mice treated with BMP-IOH-NPs and Dexa the difference to untreated AAI mice was significant. Our observations from the diaphragm motion analysis were consistent with these results. As shown in **Figure 4D**, the extent of diaphragm movement was

strongly and significantly increased in AAI mice compared to healthy controls, suggesting an effect on the elasticity of the lung as previously reported [32]. This increase was not observed upon treatment of AAI mice with BMP-IOH-NPs and Dexa, confirming the potent anti-inflammatory efficacy of the treatments. However, soluble BMP did not prevent the altered movement of the diaphragm observed in AAI mice.

We also analysed other XLF parameters that do not reflect the dynamic properties of the lung movement during the breathing cycle but that directly relate to x-ray transmission. In x-ray images, the lungs of mice treated with BMP-IOH-NPs were generally darker than those of all other treatment groups and controls, suggesting that x-ray transmission is affected by the presence of zirconium and cannot be reliably quantified (data not shown).

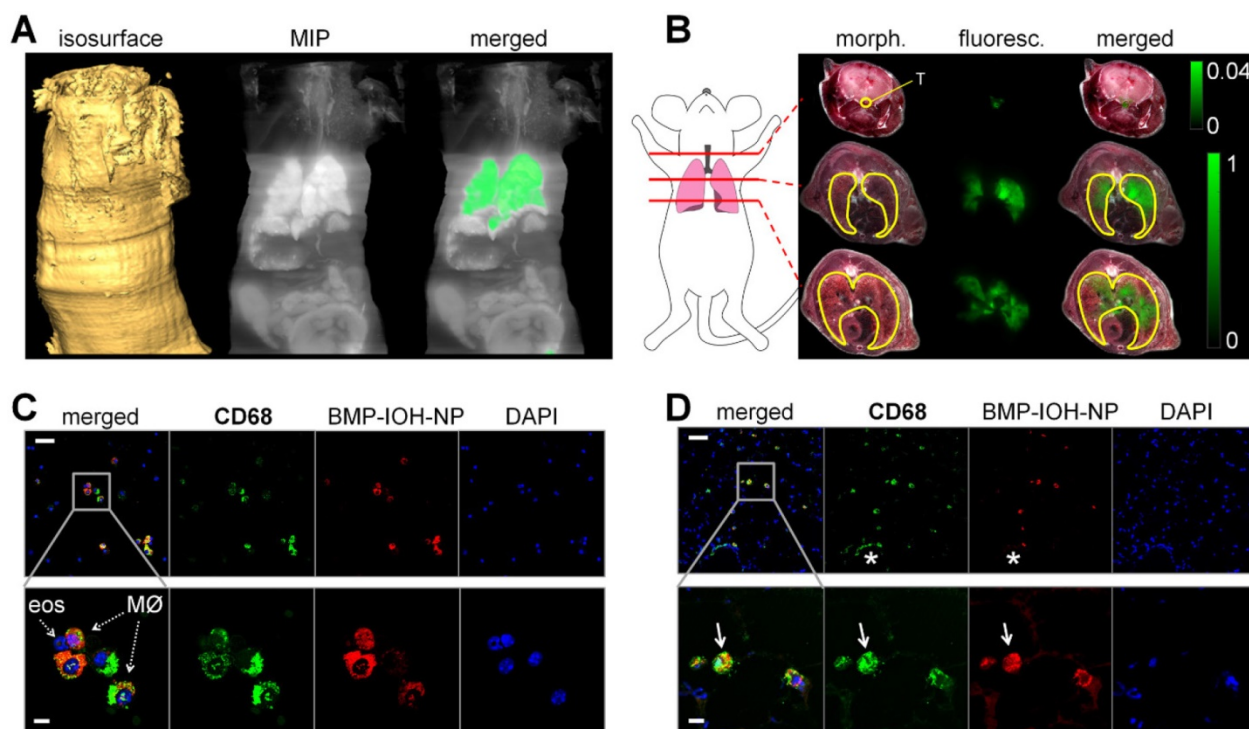


Figure 5. Uptake of BMP-IOH-NPs in the lungs of AAI mice. (A) From left to right: Isosurface reconstructed from the sliced part of the mouse. Maximum intensity projection (MIP) at the logarithmic scale of the fluorescence recorded at 810/90 nm. The same MIP with the specific ICG fluorescence (orange) segmented from phasor analysis. (B) Representative transverse whole-mouse cryosections obtained at the three planes indicated by the red lines on the cartoon (left). Morphology (morph.) and fluorescence scans (fluoresc.; green) of the same slice, as well as their overlays (merged) are shown. The fluorescence is predominantly localised in the lung (yellow line drawing) and trachea (T; yellow line drawing). Note that the signal detected at the trachea equals ~4% of the fluorescence emitted from the lungs. (C-D) Anti-CD68 staining (green) of (C) cytopspins from BALs and (D) whole-lung cryosections demonstrate uptake of BMP-IOH-NPs (red) by CD68⁺ cells, especially in the alveolar and bronchial areas (arrows). Note that BMP-IOH-NPs-positive cells were never found in dense areas of infiltrated immune cells, including the macrophages (asterisk). Nuclei are stained with DAPI (blue). Bottom panels show magnifications of the selected areas in the top panels. MØ = macrophages; eos = eosinophils. Scale bars in (C-D) represent 100 μ m in upper panels and 20 μ m in lower panels.

BMP-IOH-NPs are preferentially taken up by bronchial and alveolar macrophages

In order to assess the localisation of BMP-IOH-NPs in the lungs, a BMP-IOH-NPs-treated AAI mouse was directly frozen without prior BAL. The whole mouse was then cryosliced and the distribution of fluorescence on each cryoslice was analysed in relation to the mouse anatomy. As shown in **Figure 5A-B**, the NP-derived fluorescence was, as expected, predominantly detected in the lung tissue, while no fluorescence was present in the liver or kidneys. Although we detected some fluorescence signals in the trachea, more cryo-imaging experiments are required to validate their source. Spectral unmixing of the data shown in **Figure 5A** could not attribute this signal to ICG. Additional experiments will validate whether this signal is due to autofluorescence or ICG.

To identify the cells that take up BMP-IOH-NPs, we immunostained cytopspins from BALs as well as frozen lung tissue sections with dye-labeled anti-CD68 antibody, a widely used pan-macrophage marker. As shown in **Figure 5C**, in cytopspins from BALs of BMP-IOH-NPs-treated AAI mice, the NPs were clearly localised in CD68⁺ cells and were not

taken up by any other cells such as eosinophils, which were easily distinguished by their fragmented or donut-shaped nucleus. Similar results were observed on the whole lung cryosections (**Figure 5D**), where the BMP-IOH-NPs were clearly located within CD68⁺ inflammatory cells in alveolar spaces and in the bronchial lumen. Interestingly, we never found NPs in CD68⁺ cells located in the cell mass around bronchi and vessels, which we defined as interstitial macrophages (**Figure 5D**, asterisk).

BMP-IOH-NPs were also applied i.n. to control mice, where they were similarly taken up by CD68⁺ phagocytic cells (data not shown). Furthermore, we also i.n. applied the free fluorescent dye Dy-647 to AAI and control mice. Neither *in vivo* epi-fluorescence imaging nor microscopy showed any accumulation or uptake of free dye in the lungs of these mice (data not shown).

To analyse the cells that internalise BMP-IOH-NPs in AAI mice in more detail, we performed immunohistochemistry of whole lung cryosections with antibodies to the following protein panel: *i*) CD11c, which is expressed at high levels on most dendritic cells, but also on monocytes, macrophages and neutrophils; *ii*) ECF-L (eosinophil chemotactic

factor-L), a lectin primarily expressed on M2 macrophages; *iii*) MHCII, which is predominantly expressed on M1 macrophages; *iv*) SiglecF, an eosinophil marker; *v*) proSP-C, a marker for AT2 and *vi*) podoplanin, a marker for AT1 cells. As shown in **Figure 6**, the BMP-IOH-NPs were predominantly internalised by CD11c⁺, ECFL⁺, MHCII^{low}, SiglecF⁻, proSP-C^{low}, and podoplanin⁻ cells, which can be identified as peribronchial and alveolar M2 macrophages, as well as by a small number of proSP-C⁺ AT2 cells.

Discussion

Glucocorticoids (GC) are traditionally the drug of choice for treatment of the vast majority of immune disorders. However, along with their benefits come a number of side effects and their delivery to the site of inflammation is often difficult to predict, especially

upon systemic application. Here, we demonstrate that GCs such as BMP can be applied as fluorescent inorganic-organic hybrid nanoparticles to improve the treatment efficacy of inflammatory diseases and to allow simultaneous tracking of BMP-IOH-NPs delivery by *in vivo* epi-fluorescence imaging and microscopy. BMP-IOH-NPs are especially advantageous because they show a low material complexity and are prepared by straightforward forced hydrolysis in water, while at the same time providing a high drug loading of up to 80 wt% [23]. The potential use of clinically approved constituents, such as BMP or ICG applied here, together with the simple preparation of the NPs as an insoluble saline compound in water would advance their translation into the clinic.

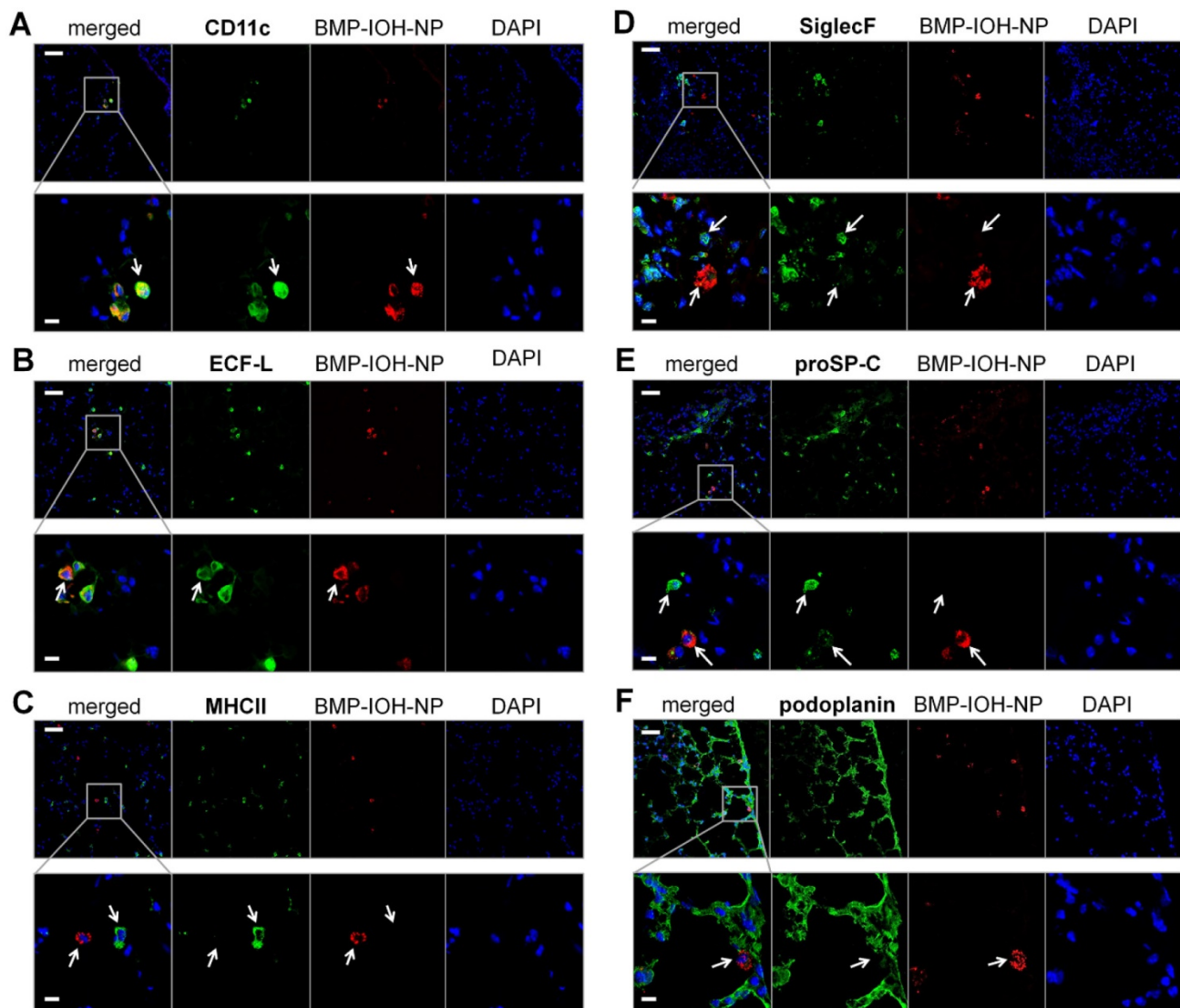


Figure 6. Analysis of BMP-IOH-NP uptake in AAI lungs. Lung cryosections were stained with antibodies targeting (A) CD11c, (B) ECF-L, (C) MHC II, (D) SiglecF, (E) proSP-C and (F) podoplanin (each in green). Cells that internalised BMP-IOH-NPs (red; arrows) were identified as CD11c⁺, ECFL⁺, MHC II^{low}, SiglecF⁻ peribronchial and alveolar M2 macrophages as well as a few proSP-C⁺ AT2 cells. Nuclei are stained with DAPI (blue). Bottom panels show magnifications of the selected areas in the top panels. Scale bars represent 100 μ m in upper panels and 20 μ m in lower panels.

In our experiments, BMP-IOH-NPs resulted in improved therapeutic efficacy both *in vitro* and *in vivo* when compared to free BMP. *In vitro*, this effect was especially prominent at concentrations of the active compound between 10^{-7} and 10^{-8} M, at which BMP-IOH-NPs reduced IL-6 production in LPS-stimulated MH-S cells even more than both free control drugs, Dexa and BMP. In mice with sterile paw inflammation, we observed a clear decrease in paw swelling upon intraperitoneal treatment of the mice with BMP-IOH-NPs, with excellent tolerance in the treated animals. Matching results were obtained *ex vivo* by both paw weight measurement and CT imaging, which revealed reduced paw weights and volumes, respectively, in the BMP-IOH-NPs-treated mice, confirming their high efficacy for treatment of inflammation.

In the model of OVA-induced AAI using both traditional methods such as BAL cell count and histology as well as *in vivo* x-ray-based lung function measurements, we showed that i.n.-instilled BMP-IOH-NPs *i)* efficiently reduced AAI symptoms, like infiltration of eosinophils into the lung tissue, to levels comparable with that of Dexa-treated mice and healthy controls, and *ii)* clearly exhibited a higher efficacy than soluble BMP applied at the same dose. Consistently, XLF parameters “relative inspiration time” t_{in} and diaphragm motion revealed that only mice treated with BMP-IOH-NPs or Dexa, but not those treated with soluble BMP, showed an anti-inflammatory effect with values similar to those of healthy controls. T_{in} represents the ratio of time of inspiration to the duration of the whole breathing sequence and is normally decreased in AAI mice due to the longer exhalation period caused by the reduced elastic recoil of the lung tissue in these animals [32]. In healthy animals, inspiration involves active contraction of the diaphragm and the intercostal muscles while exhalation occurs more passively and depends on the elastic recoil of the lung. When the latter is lost, AAI mice need to put much more effort into pushing the air out of the lung, which leads to longer exhalation (and shorter relative inspiration) times as well as stronger movement of the diaphragm [30,32]. This is in agreement with our observations that vehicle-treated AAI mice whose lungs are infiltrated by a high number of immune cells showed dramatically reduced parameter t_{in} , which was improved upon treatment with BMP-IOH-NPs and Dexa and to a lesser extent with soluble BMP. In accordance with our previous observations [32], we also showed that the diaphragm movement calculated from the x-ray movies was aberrantly strong in AAI mice. In mice treated with BMP-IOH-NPs or Dexa, but not with soluble BMP, this aberrant movement was reduced to

a level resembling that of healthy controls. These results are highly consistent with all other data obtained in this study and confirm the high efficacy of BMP-IOH-NPs for treatment of inflammation.

The XLF parameters assessed in our study—the relative inspiration time t_{in} and diaphragm motion—are both “dynamic” parameters that reflect the kinetics of the lung movement during the breathing cycle. In evaluations of the lung “transparency” over a breathing cycle, we previously showed that AAI mice also demonstrate changes in other XLF parameters that reflect differences in air content due to thickening of the lung tissue [30]. Interestingly, in our experiments, these parameters seem to be affected by the presence of zirconium, because BMP-IOH-NPs influenced x-ray transmission in the lung region and resulted in overall darker x-ray images of BMP-IOH-NPS-treated lungs compared to untreated lungs (data not shown). It is thus possible that treatment with BMP-IOH-NPs impacted other XLF parameters too, which, however, could not be recognized (or quantified) due to the overall increased x-ray absorbance caused by the NPs. At the same time, this observation suggests that BMP-IOH-NP-loaded macrophages could potentially also be visualised by high-resolution x-ray technologies, or used for x-ray-based virtual histology, as previously described for barium-loaded NPs [38]. Such an approach would allow 3D analysis of the homing sites of loaded macrophages in respect to local anatomical alterations.

Our XLF data as well as paw volume measurements by CT delivered valuable parameters to assess GC efficacy and thus notably showed the advantages of using imaging modalities for monitoring the progression of inflammatory disease. In particular, non-invasive low-dose CT facilitates longitudinal assessment of the course and extent of inflammation. While MRI could potentially be used to monitor progression of inflammation, this imaging modality requires long scanning times and complex infrastructure and delivers a much lower resolution in comparison to x-ray-based technologies.

The route of administration undoubtedly affects the biodistribution and thus possibly also the efficacy of therapeutic compounds. In our experiments performed in the paw inflammation model, we chose an i.p. application since it is less burdensome to the animals than intravenous (i.v.) application, especially upon repetitive administration (here on three consecutive days). I.v. application could possibly generate divergent results, since it is well known that i.v.-applied particles are usually rapidly taken up by the mononuclear phagocyte system (MPS) and accumulate in the liver. This often reduces their time

of circulation and lowers their accumulation at the desired sites [39]. Furthermore, in our previous studies, we i.v.-applied analogous IOH-NP with the composition $[\text{GdO}]^+[\text{ICG}]^-$ and observed their accumulation in the liver within ~5 h after injection [22]. Whether this would be the case for BMP-IOH-NPs and to what extent it would affect their therapeutic effects remains to be analysed.

In this context, the unique trait of the BMP-IOH-NPs presented here is their simple composition that incorporates fluorescent dye molecules (Dy-647 or ICG) together with the therapeutic compound, allowing for simultaneous monitoring of their biodistribution and drug delivery. This was well demonstrated in the AAI model, for which we used hairless SKH-1 mice to minimize loss of fluorescence signals. Our longitudinal *in vivo* fluorescence imaging experiments demonstrate that the NPs are quickly and efficiently delivered to the lung, where they accumulate for at least 24 h, which apparently was a sufficient period for the drug to take effect. This information is especially important as deposition of inhaled drugs and in particular of NPs in the lung is difficult to predict as it depends on a variety of factors such as particle size, composition, shape or charge, but also on breathing rate or structural properties of the lung [40]. The advantage of the incorporated fluorescent compound was particularly apparent by additionally revealing a “loss” of some NPs in the pharynx and oesophagus. Because mucus over-production is a symptom of asthma, we assume that these signals were caused by part of the NPs sticking to the mucus in the upper airways and being continually swallowed and excreted. Not only does this demonstrate the advantage of monitoring biodistribution, it also confirms the high potency of the BMP-IOH-NPs despite this apparent loss of NPs. An alternative application route that may prevent loss of NPs in the mucus could be by intratracheal instillation. However, this method is much more invasive than intranasal delivery, requires long anaesthesia times and usually leads to irritation and sometimes even inflammation of the airways. It was therefore not used for BMP-IOH-NPs application.

The fluorescence lifetime measurements performed in our study offer an additional advantage to unravel the biodistribution of the probe by showing that, especially at early time points after application, low concentrations of the probe are present in the entire body or at least the scanned area (upper thorax). Because fluorescence lifetime is independent of dye/particle concentration, we believe that at early time points post instillation there is a minor portion of either the intact NPs or the released fluorescent dye present in the circulation with blood clearance times

below 4 h.

We showed that i.n.-applied BMP-IOH-NPs, with an average size of about 30 nm, are taken up by peribronchial and alveolar macrophages. Our extensive staining protocol identified these macrophages as M2 macrophages. *In vitro*, using the MH-S cell line, we found that the internalisation process occurs very fast and could be detected as early as 10 min after incubation. Electron microscopy showed a typical internalisation pathway, with the particles ending up in large vesicles, which is known from other NPs [41]. Similar uptake of intranasally applied 100 nm polystyrene NPs by the bronchial and alveolar macrophages was already observed in our previous studies [37].

Recently, it has been shown that alveolar type 2 (AT2) cells, rather than immune cells, seem to be major players in the response of AAI lungs to GCs [42]. This is especially interesting because, despite the minimal uptake by AT2 cells, we observed a high treatment efficacy of BMP-IOH NPs, suggesting that macrophages that take up BMP-IOH-NPs must also play a significant role in the transfer of GC efficacy in AAI and probably in general in the treatment of inflammation. Similar BMP-IOH-NPs were recently applied in a mouse model of multiple sclerosis and compared to free GC showed an increased specificity for phagocytic cells but not for T cells or brain endothelial cells, while retaining full therapeutic efficacy [17]. One explanation for the high efficacy of BMP-IOH-NPs could be that macrophages, which internalise the NPs, act as a depot, slowly releasing the drug to the environment and allowing it to act on receiver-cells, such as AT2 cells or eosinophils. A similar phenomenon has already been described in the context of tumour therapy by the group of Weissleder, who showed that therapeutic fluorescent NPs promote long drug circulation and alter accumulation by directing cellular uptake toward tumour-associated macrophages (TAMs). TAMs were suggested to serve as a local drug depot that accumulates significant vehicle from which the drug payload gradually releases to neighbouring tumour cells [43]. These findings support the notion that encapsulation of the drug in NPs, such as BMP-IOH-NPs, that can then be easily taken up by macrophages can improve therapeutic efficacy.

One of the most important benefits of IOH-NPs is their simple formulation based on the inorganic cation $[\text{ZrO}]^{2+}$ used in this study and organic anion(s), here the combination of $[\text{DUT}]^{2-}$ and $[\text{BMP}]^{2-}$, together with simple synthesis by precipitation in aqueous solution [23]. Each component can be easily replaced to modify the particle function and field of application. In our previous studies, we have already shown

that IOH-NPs with the composition $[\text{GdO}]^+[\text{ICG}]^-$ can be efficiently detected by MRI. The replacement of $[\text{ZrO}]^{2+}$ with $[\text{GdO}]^+$ could thus create an anti-inflammatory probe that can be tracked by MRI in addition to fluorescence imaging. This is especially interesting as the application of fluorescence imaging in patients is very restricted due to the limited penetration depth. A hybrid probe for fluorescence and MR imaging could therefore be used in both preclinical and clinical approaches for a comprehensive understanding of the biodistribution of the drug.

Analogously, the organic compound of IOH-NPs can also be exchanged with other organic anion(s), as has been already shown, e.g., for $[\text{ZrO}]^{2+}[\text{FdUMP}]^{2-}$, which contains an active cytostatic agent instead of anti-inflammatory BMP [23]. At the same time, IOH-NPs offer the possibility of integrating several organic compounds in the same particle, such as the fluorescent dyes $[\text{DUT}]^{2-}$ or $[\text{ICG}]^{2-}$ used here together with the inflammatory agent $[\text{BMP}]^{2-}$. Similarly, different drugs can also be incorporated in one particle, which could potentially increase their efficacy and field of action.

To move toward the goal of clinical translation of IOH-NPs as potential macrophage-mediated drug delivery systems, in particular of BMP-IOH-NPs for the treatment of inflammation, it is still necessary to evaluate their exact underlying mechanisms as well as their drug release profiles, especially in *in vivo* settings.

Conclusions

We show that glucocorticoids such as BMP applied in the form of fluorescent IOH-NPs allow more efficient treatment of inflammatory disease than the equivalent free drug and provide simultaneous non-invasive monitoring of NP delivery by optical imaging.

Abbreviations

AAI: allergic airway inflammation; AT2 cells: alveolar type 2 cells; BAL: bronchoalveolar lavage; BMP: betamethasone phosphate; BMP-IOH-NPs: BMP containing inorganic-organic hybrid nanoparticles; CT: computed tomography; Dexa: dexamethasone; DUT: DY-647-dUTP; GC: glucocorticoid, ICG: indocyanine green; IL-6: Interleukin-6; i.n.: intranasal; i.p.: intraperitoneal; i.v.: intravenous; LPS: lipopolysaccharide; MRI: magnetic resonance imaging; IRF: near infrared fluorescence; NP: nanoparticle; NC: normalised counts; OVA: ovalbumin; SD: standard deviation; TAM: tumour-associated macrophage; XLF: x-ray-based lung function

Acknowledgements

We thank the Max-Planck Institute for Experimental Medicine for financial support. We thank Bärbel Heidrich, Sarah Garbode, Sabine Wolfgramm, Bettina Jeep, Roswitha Streich, Torben Ruhwedel and Hannah Puchala for excellent technical assistance. We also thank Prof. Philipp Ströbel for support with histological analysis and Maximilian Koch and Prof. Vasilis Ntziachristos for support with imaging of whole mouse cryosections. J.G.H. and C.F. as well as F.A. acknowledge the German Research Society (Deutsche Forschungsgemeinschaft; DFG) for equipment. D.G. and V.N. acknowledge funding by the German Research Society (Deutsche Forschungsgemeinschaft; DFG), Sonderforschungsbereich-824 (SFB-824), sub-project Z3.

Competing Interests

The authors have declared that no competing interest exists.

References

- Medzhitov R. Origin and physiological roles of inflammation. *Nature*. 2008; 454: 428-435.
- Barnes PJ. Immunology of asthma and chronic obstructive pulmonary disease. *Nat Rev Immunol*. 2008; 8: 183-192.
- Barnes PJ. How corticosteroids control inflammation: Quintiles prize lecture 2005. *Br J Pharmacol*. 2006; 148: 245-254.
- Barnes PJ. Mechanisms and resistance in glucocorticoid control of inflammation. *J Steroid Biochem Mol Biol*. 2010; 120: 76-85.
- van der Velden VH. Glucocorticoids: mechanisms of action and anti-inflammatory potential in asthma. *Mediators Inflamm*. 1998; 7: 229-237.
- Spahn JD, Covar R. Glucocorticoid therapy in asthma. In: Lieberman P, Anderson J.A. (eds), *Allergic Diseases. Current Clinical Practice*. Humana Press; 2007: 385-401
- Rhen T, Cidlowski JA. Antiinflammatory action of glucocorticoids—new mechanisms for old drugs. *N Engl J Med*. 2005; 353: 1711-1723.
- Puri A, Loomis K, Smith B, et al. Lipid-based nanoparticles as pharmaceutical drug carriers: from concepts to clinic. *Crit Rev Ther Drug Carrier Syst*. 2009; 26: 523-580.
- Zhang Y, Huang Y, Li S. Polymeric Micelles: Nanocarriers for cancer-targeted drug delivery. *AAPS PharmSciTech*. 2014; 15: 862-871.
- Kumari A, Singla R, Guliani A, Yadav SK. Nanoencapsulation for drug delivery. *EXCLI J*. 2014; 13: 265-286.
- Min Y, Caster JM, Eblan MJ, Wang AZ. Clinical translation of nanomedicine. *Chem Rev*. 2015; 115: 11147-11190.
- Pillai G. Nanomedicines for Cancer Therapy: An update of FDA approved and those under various stages of development. *SOJ Pharm Pharm Sci*. 2014; 1: 13.
- Adler-Moore J, Proffitt RT. AmBisome: liposomal formulation, structure, mechanism of action and pre-clinical experience. *J Antimicrob Chemother*. 2002; 49 Suppl 1: 21-30.
- Thakor AS, Jokerst JV, Ghanouni P, Campbell JL, Mittra E, Gambhir SS. Clinically approved nanoparticle imaging agents. *J Nucl Med*. 2016; 57: 1833-1837.
- Ratemi E, Sultana Shaik A, Al Faraj A, Halwani R. Alternative approaches for the treatment of airway diseases: focus on nanoparticle medicine. *Clin Exp Allergy*. 2016; 46: 1033-1042.
- Quan L, Zhang Y, Crieleard BJ, et al. Nanomedicines for inflammatory arthritis: head-to-head comparison of glucocorticoid-containing polymers, micelles and liposomes. *ACS Nano*. 2014; 8: 458-466.
- Montes-Cobos E, Ring S, Fischer HJ, et al. Targeted delivery of glucocorticoids to macrophages in a mouse model of multiple sclerosis using inorganic-organic hybrid nanoparticles. *J Control Release*. 2017; 245: 157-169.
- Matsuo Y, Ishihara T, Ishizaki J, Miyamoto K, Higaki M, Yamashita N. Effect of betamethasone phosphate loaded polymeric nanoparticles on a murine asthma model. *Cell Immunol*. 2009; 260: 33-38.
- Kenyon NJ, Bratt JM, Lee J, et al. Self-assembling nanoparticles containing dexamethasone as a novel therapy in allergic airways inflammation. *PLoS One*. 2013; 8: e77730.
- Key J, Leary JF. Nanoparticles for multimodal *in vivo* imaging in nanomedicine. *Int J Nanomedicine*. 2014; 9: 711-726.

21. Lacroix L-M, Delpech F, Nayral C, Lachaize S, Chaudret B. New generation of magnetic and luminescent nanoparticles for in vivo real-time imaging. *Interface Focus*. 2013; 3: 20120103.
22. Poś M, Tower RJ, Napp J, et al. Multimodal [GdO]⁺[ICG]- nanoparticles for optical, photoacoustic, and magnetic resonance imaging. *Chem Mater*. 2017; 29: 3547-3554.
23. Heck JG, Napp J, Simonato S, et al. Multifunctional phosphate-based inorganic-organic hybrid nanoparticles. *J Am Chem Soc*. 2015; 137: 7329-7336.
24. Roming M, Lünsdorf H, Dittmar KEJ, Feldmann C. ZrO(HPO₄)_{1-x}(FMN)_x: Quick and easy synthesis of a nanoscale luminescent biomarker. *Angew Chem Int Ed*. 2010; 49: 632-637.
25. Dilworth JR, Pascu SI. The chemistry of PET imaging with zirconium-89. *Chem Soc Rev*. 2018; 47: 2554-2571.
26. Packham DK, Kosiborod M. Pharmacodynamics and pharmacokinetics of sodium zirconium cyclosilicate [ZS-9] in the treatment of hyperkalemia. *Expert Opin Drug Metab Toxicol*. 2016; 12: 567-573.
27. Reynolds ES. The use of lead citrate at high pH as an electron-opaque stain in electron microscopy. *J Cell Biol*. 1963; 17: 208-212.
28. Gadó K, Gigler G. Zymosan inflammation: A new method suitable for evaluating new antiinflammatory drugs. *Agents Actions*. 1991; 32: 119-121.
29. Napp J, Dullin C, Müller F, et al. Time-domain in vivo near infrared fluorescence imaging for evaluation of matriptase as a potential target for the development of novel, inhibitor-based tumor therapies. *Int J Cancer*. 2010; 127: 1958-1974.
30. Dullin C, Markus MA, Larsson E, Tromba G, Hülsmann S, Alves F. X-Ray based lung function measurement—a sensitive technique to quantify lung function in allergic airway inflammation mouse models. *Sci Rep*. 2016; 6: 36297.
31. Schindelin J, Arganda-Carreras I, Frise E, et al. Fiji: an open-source platform for biological-image analysis. *Nat Methods*. 2012; 9: 676-682.
32. Markus MA, Borowik S, Reichardt M, Tromba G, Alves F, Dullin C. X-ray-based lung function measurement reveals persistent loss of lung tissue elasticity in mice recovered from allergic airway inflammation. *Am J Physiol Lung Cell Mol Physiol*. 2017; 313: L763-L771.
33. Fereidouni F, Gorpas D, Ma D, Fatakdawala H, Marcu L. Rapid fluorescence lifetime estimation with modified phasor approach and Laguerre deconvolution: a comparative study. *Methods Appl Fluoresc*. 2017; 5: 035003.
34. Cutrale F, Trivedi V, Trinh LA, et al. Hyperspectral phasor analysis enables multiplexed 5D in vivo imaging. *Nat Methods*. 2017; 14: 149-152.
35. Symvoulidis P, Pérez CC, Schwaiger M, Ntziachristos V, Westmeyer GG. Serial sectioning and multispectral imaging system for versatile biomedical applications. *IEEE 11th International Symposium on Biomedical Imaging (ISBI)*. 2014; 890-893.
36. Hammer, Ø.; Harper, D. A. T. I.; Ryan, P. D. PAST: Paleontological statistics software package for education and data analysis. *Palaeontol Electron*. 2001; 4: 1-9.
37. Markus MA, Napp J, Behnke T, et al. Tracking of inhaled near-infrared fluorescent nanoparticles in lungs of SKH-1 mice with allergic airway inflammation. *ACS Nano*. 2015; 9: 11642-11657.
38. Dullin C, dal Monego S, Larsson E, et al. Functionalized synchrotron in-line phase-contrast computed tomography: a novel approach for simultaneous quantification of structural alterations and localization of barium-labelled alveolar macrophages within mouse lung samples. *J Synchrotron Radiat*. 2015; 22: 143-155.
39. Almeida JPM, Chen AL, Foster A, Drezek R. In vivo biodistribution of nanoparticles. *Nanomed*. 2011; 6: 815-835.
40. Carvalho TC, Peters JL, Williams RO. Influence of particle size on regional lung deposition - What evidence is there? *Int J Pharm*. 2011; 406: 1-10.
41. Kevadiya BD, Woldstad C, Ottemann BM, et al. Multimodal theranostic nanoformulations permit magnetic resonance bioimaging of antiretroviral drug particle tissue-cell biodistribution. *Theranostics*. 2018; 8: 256-276.
42. Kláßen C, Karabinskaya A, Dejager L, et al. Airway epithelial cells are crucial targets of glucocorticoids in a mouse model of allergic asthma. *J Immunol*. 2017; 199: 48-61.
43. Miller MA, Zheng Y-R, Gadde S, et al. Tumour-associated macrophages act as a slow-release reservoir of nano-therapeutic Pt(IV) pro-drug. *Nat Commun*. 2015; 6: 8692.